Primordial Non-Gaussianity: Simulations

Jaafar Chakrani

Research Project Report

Declaration of integrity regarding plagiarism

I, Jaafar Chakrani, certify on my honor that:

- The results described in this report are the results of my own work.

- I am the author of this report.

- I have not used third party sources or results without clearly citing them and reference them according to the recommended bibliographical rules.

I declare that this work cannot be suspected of plagiarism.

Jaafar Chakrani

Acknowledgements

Résumé

Dans ce rapport, nous commençons par effectuer une revue de modèles inflationnaires qui génèrent des non-gaussianités dans la distribution des fluctuations de métrique primordiales ζ. Cette non-gaussianité ne correspond pas tout le temps à la paramétrisation classique par f_{NL}. Nous nous intéressons en particulier à des proéminences non-gaussiennes sous forme de pics spatiaux sur des régions compactes dans les réalisations de ζ. Pour ce faire, nous généralisons la prescription f_{NL} à des fonctions non-linéaires $F_{NL}(\zeta_G)$. Une étude est conduite pour déterminer les effets statistiques sur ζ par différents modèles de F_{NL} en distinguant deux situations: lorsque ces proéminences sont corrélées aux fluctuations de métrique primordiales issues de l'inflation et lorsqu'elles ne le sont pas, comme lors du préchauffage. Ceci peut être lié aux observables cosmologiques par des simulations numériques, notamment avec des simulations à mailles de l'univers primordial qui génèrent ζ et le logiciel mass-Peak Patch qui produit des catalogues de halos de matière noire ainsi que des cartes de ciel. Le lien entre les deux simulations est établi. Dans le cadre de ces proéminences, nous explorons une méthode numérique potentielle de séparer les composantes non-gaussiennes du champ gaussien appelée Analyse en Composantes Indépendantes. Nous effectuons des tests simplifiés sur des cas liés au modèle de proéminence pour séparer des pics du signal gaussien, et ceci avec différentes mesures de non-gaussianités.

Abstract

In this report we review inflationary models where non-Gaussianity in the primordial curvature perturbation ζ emerges in a way that does not necessarily match the commonly-used f_{NL} parameterization. We are particularly interested in non-Gaussian prominence in the shape of peaks appearing in the real-space ζ field. We generalize the f_{NL} prescription with a non-linear function $F_{NL}(\zeta_G)$ and study the effect of different F_{NL} models on the statistics of the curvature perturbation. To do so we distinguish between the contributions that are correlated and the ones that are uncorrelated with the inflaton-sourced component of ζ, as is the case in massless preheating. This can be linked to cosmological observables via numerical simulations, and particularly from the early universe lattice simulations that give curvature perturbation to the mass-Peak Patch software which does a fast generation of halo catalogues and full-sky maps. As a potential way to characterize non-Gaussianity, especially in this prominence picture, we conduct simplified tests of Independent Component Analysis to separate non-Gaussian peaks from a Gaussian signal using different measures of non-Gaussianity.

Contents

List of Figures

Introduction

The origin of the primordial density fluctuations is a key issue in understanding the physics of the early Universe. In the inflationary paradigm [3, 4, 5], the generated quantum fluctuations are seeds to the density fluctuations. The exact process that yields these fluctuations however remains unknown. The shape of the inflaton potential, the fields other than the inflaton participating in inflation and so on are thus far a mystery. Recent measurements of the Cosmic Microwave Background (CMB) and the Large-Scale Structure (LSS) constrain the possible inflationary scenarios. The observable universe seems to be consistent with an extremely simple set of initial conditions. The seed of the observed cosmological inhomogeneity is a Gaussian primordial curvature perturbation ζ defined by a nearly scale-invariant power spectrum. This is confirmed with the current CMB measurements with Planck satellite [6], but deviations from this Gaussian profile within the Planck bounds are still a possibility. In single-field slow-roll inflation, non-Gaussianity is predicted to be very small and unobservable in the foreseen future. Large non-Gaussianity may arise when the interactions during inflation are significant. Therefore, the search for primordial non-Gaussianity is a strong probe and a unique opportunity to characterize the interactions that occurred during inflation.

To understand these non-Gaussian effects, it is of great interest to study the statistics of the perturbations arising in different inflation models, especially the less understood ones including complicated dynamics. Numerical simulations have been very helpful in complementing observations. In particular, N-body simulations were conducted with f_{NL} non-Gaussian initial conditions (e.g. [7, 8, 9]) or even more general ones specified by a given bispectrum [10]. We are interested here in non-Gaussianity that does not match the f_{NL} type, as non-trivial non-Gaussianity may arise in many inflationary models. The bispectrum is a widely-used measure of non-Gaussianity which can distinguish between different shapes issued from different inflation models (e.g. see Ref. [11] for a review). It is the simplest measure after the power spectrum and a detection of a non-vanishing bispectrum would confirm non-Gaussianity. How-

ever, it can by no means characterize non-Gaussianity. Actually, even going after the trispectrum and higher-order polyspectra would not be enough for the simple reason that in general moments do not define distributions. We explore Independent Component Analysis (ICA) as a potential way to measure non-Gaussianity of a given signal. It is a blind source separation problem commonly applied in image processing and speech separation, to cite a few.

In this report, we review inflation and some of the key inflationary and post-inflationary models (Ch. 1) that can generate significant non-Gaussianity not necessarily matching the f_{NL} type (Ch. 2). We then propose primordial curvature perturbation models that could be used as initial conditions for N-body simulations (Ch. 3). Finally, we explore ICA and test it in some situations of interest (Ch. 4).

Chapter 1

The Early Universe: Overview

The inflationary paradigm is usually regarded as the most promising theory describing the early stages of the evolution of the universe. In addition to solving some of the Hot Big Bang model problems, it offers a specific mechanism, namely quantum fluctuations, for generating the primordial cosmological perturbations that are observed on the CMB and seed the late-time structures. We start by deriving the generic single-field slow-roll inflation equations in a homogeneous universe (Sec. 1.1.1) and studying its quantum perturbations (Sec. 1.1.2). Variations of this standard scenario are explored (Sec. 1.1.3, 1.1.4 and 1.2), and links with cosmological observables are highlighted (Sec. 1.3).

1.1 Inflation

1.1.1 Background equations

We assume a Friedmann–Lemaitre–Robertson–Walker (FLRW) metric of a flat universe:

$$ds^2 = -dt^2 + a^2(t)\delta_{ij}dx^i dx^j.$$

Throughout this report, we will use natural units $c = \hbar = 1$ and set the Planck mass $M_P \equiv (8\pi G)^{1/2} = 1$.

This metric describes an expanding flat, homogeneous and isotropic universe with the scale factor $a(t)$. The Hubble parameter is related to the scale factor by: $H \equiv \dot{a}/a$. The evolution is governed by the Einstein equations

$$G_{\mu\nu} = T_{\mu\nu},$$

where $G_{\mu\nu}$ is the Einstein tensor, describing the the space-time structure, and $T_{\mu\nu}$ is the energy-momentum tensor, describing the matter occupying the space-time. At the

background level, the energy-momentum tensor can be considered that of a perfect fluid (in a comoving frame with the fluid) and be expressed:

$$T^\mu{}_\nu = \text{diag}(-\rho, p, p, p) \tag{1.1}$$

This gives the well-known Friedmann equations:

$$H^2 = \frac{1}{3}\rho \tag{1.2}$$

and

$$\frac{\ddot{a}}{a} = -\frac{1}{6}(\rho + 3p). \tag{1.3}$$

The energy conservation equation (or the continuity equation) can be derived by combining (1.2) and (1.3):

$$\dot{\rho} + 3H(\rho + p) = 0. \tag{1.4}$$

It can also be obtained from the $\nu = 0$ component of the energy-momentum tensor conservation

$$\nabla_\mu T^\mu{}_\nu = 0. \tag{1.5}$$

The simplest model of inflation involves a single scalar field ϕ called the inflaton. Its dynamics coupled to gravity are given by the action:

$$S = \int d^4x \sqrt{-g} \left[\frac{1}{2}R + \frac{1}{2}g^{\mu\nu}\partial_\mu\phi\partial_\nu\phi - V(\phi) \right] \tag{1.6}$$

where R is the Ricci scalar and $V(\phi)$ is the inflation potential that describes the self-interactions of the inflaton. By varying the matter Lagrangian part $\mathcal{L}_m \equiv \frac{1}{2}g^{\mu\nu}\partial_\mu\phi\partial_\nu\phi - V(\phi)$ of (1.6) with respect to $g^{\mu\nu}$, the energy-momentum tensor of the scalar field is:

$$T_{\mu\nu} = -\frac{2}{\sqrt{-g}}\frac{\delta\left(\sqrt{-g}\mathcal{L}_m\right)}{\delta g^{\mu\nu}} = \partial_\mu\phi\partial_\nu\phi - g_{\mu\nu}\left[\frac{1}{2}g^{\rho\sigma}\partial_\rho\phi\partial_\sigma\phi + V(\phi)\right].$$

Consequently, the pressure and the density can be matched with (1.1):

$$\rho = -T^0{}_0 = \frac{1}{2}\dot{\phi}^2 + \frac{1}{2}\frac{(\nabla\phi)^2}{a^2} + V, \tag{1.7}$$

$$p = \frac{1}{3}T^i{}_i = \frac{1}{2}\dot{\phi}^2 - \frac{1}{6}\frac{(\nabla\phi)^2}{a^2} - V. \tag{1.8}$$

The field equation of motion is:

$$\frac{\delta S}{\delta\phi} = \frac{1}{\sqrt{-g}}\partial_\mu\left(\sqrt{-g}\partial^\mu\phi\right) + \frac{\partial V}{\partial\phi} = 0$$

4

which gives the Klein-Gordon equation:

$$\ddot{\phi} - \frac{1}{a^2}\Delta\phi + 3H\dot{\phi} + \frac{\partial V}{\partial \phi} = 0. \tag{1.9}$$

Considering a homogeneous background, such that $\phi(t, \mathbf{x}) = \phi(t)$, these equations become:

$$p = \frac{1}{2}\dot{\phi}^2 - V,$$

$$\rho = \frac{1}{2}\dot{\phi}^2 + V,$$

$$\ddot{\phi} + 3H\dot{\phi} + \frac{\partial V}{\partial \phi} = 0,$$

and (1.2) becomes:

$$3H^2 = V + \frac{1}{2}\dot{\phi} \tag{1.10}$$

By differentiating and using the field motion equation, we obtain:

$$2\dot{H} = -\dot{\phi}^2. \tag{1.11}$$

Let us formulate the slow-roll approximation of inflation. We first assume that the expansion is almost exponential:

$$\frac{|\dot{H}|}{H^2} \ll 1 \tag{1.12}$$

which is equivalent, using (1.3), to

$$3H^2 \approx V. \tag{1.13}$$

Assuming that this approximated expression also holds for its low derivatives and using (1.11), it becomes:

$$3H\dot{\phi} \approx -V'(\phi). \tag{1.14}$$

It follows that:

$$\epsilon \equiv \frac{1}{2}\left(\frac{V'}{V}\right)^2 \ll 1. \tag{1.15}$$

This is equivalent to neglecting the $\ddot{\phi}$ term in the field equation of motion: $|\ddot{\phi}| \ll 3H|\dot{\phi}|, |V'|$, which requires the smallness of $|\ddot{\phi}|/|H\dot{\phi}|$ and can be expressed in terms of the potential as:

$$|\eta| \ll 1 \quad \text{where} \quad \eta \equiv \frac{V''}{V}. \tag{1.16}$$

Finally, in the slow-roll approximation, the background evolution is described by:

$$H^2 \approx \frac{1}{3}V \approx \text{ const}, \tag{1.17}$$

$$3H\dot{\phi} \approx -V'. \tag{1.18}$$

1.1.2 The inhomogeneous universe

During inflation, cosmological perturbations arise from quantum fluctuations. Their study splits the background and the perturbations, which is not unique and this freedom is called a choice of *gauge*. In the homogeneous universe, as seen in the previous section, the definition of FLRW metric introduced the coordinates t and $\mathbf{x}$. The threading (timelike wordline of constant $\mathbf{x}$) corresponds to a comoving free-falling observer which defines an isotropic expansion. The slicing (spacelike hypersurface of constant t) is orthogonal to the threading, and all the quantities on it are homogeneous. When perturbations are considered, the threading and the slicing of the perturbed universe are no longer unique and the coordinates with these properties are impossible to find. One thus requires that in the limit of zero perturbation the FLRW case is recovered. And a coordinate choice that satisfies this condition is a gauge.

One gauge choice consists in parameterizing the metric using ψ as [12]:

$$ds^2 = -dt^2 + a(t)e^{\psi(t,\mathbf{x})}dx^2, \tag{1.19}$$

which defines a local scale factor $\tilde{a}(\mathbf{x},t) \equiv a(t)e^{\psi(\mathbf{x},t)}$. There are different slicing possibilities of the space-time with different ψ. For instance, the spatially flat gauge corresponds to $\psi = 0$. In general, ψ can be interpreted as the perturbation of the scale factor as $\psi = \delta \ln \tilde{a} = \delta\tilde{a}/a$ so that to first order $\tilde{a}(t,\mathbf{x}) \approx a(t)(1 + \psi(\mathbf{x},t))$.

A specific gauge choice consists in setting the time slices to have uniform energy density ($\delta\rho = 0$), denoting ψ on this slicing by $-\zeta$, where ζ defines the *primordial curvature perturbation*. Actually, ζ can be defined as a gauge-invariant quantity, so that it is independent of the choice of time-slicing [12].

To keep things simple, we only consider the perturbed inflaton field and and ignore the metric perturbations. The inflaton writes:

$$\phi(\mathbf{x},t) = \phi(t) + \delta\phi(\mathbf{x},t). \tag{1.20}$$

In the slow-roll approximation, the perturbation $\delta\phi$ evolves as a free massless field, and its equation of motion in momentum space using the Fourier expansion

$$\delta\phi(\mathbf{k},t) \equiv \int d^3x \delta\phi(\mathbf{x},t)e^{i\mathbf{k}\cdot\mathbf{x}}$$

is:

$$\ddot{\delta\phi}(\mathbf{k}, t) + 3H\dot{\delta\phi}(\mathbf{k}, t) + \frac{k^2}{a^2}\delta\phi(\mathbf{k}, t) = 0. \tag{1.21}$$

To quantize the perturbations, $\delta\phi$ is decomposed

$$\delta\phi(\mathbf{k}, t) = u(\mathbf{k}, t)a_{\mathbf{k}} + \text{h.c.}$$

where u is the mode function and $a_{\mathbf{k}}^{\dagger}$ and $a_{\mathbf{k}}$ are respectively the creation and annihilation operators. The mode function can be written down explicitly by solving (1.21) in conformal time $d\eta \equiv dt/a$, supposing that $H \approx \text{const.}$ [13]:

$$u(\mathbf{k}, \eta) = \frac{H}{\sqrt{2k^3}}(k\eta - i)e^{-ik\eta}. \tag{1.22}$$

It is known as the Bunch-Davies mode function. We can now compute the *dimensionless power spectrum* of the perturbation $\Delta_{\delta\phi}$ which is defined by:

$$\langle \delta\phi(\mathbf{k}, \eta)\delta\phi(\mathbf{k}', \eta) \rangle = (2\pi)^3\delta^D(\mathbf{k} + \mathbf{k}')\Delta_{\delta\phi}(k) \tag{1.23}$$

and we have

$$\Delta_{\delta\phi}(k) = \frac{H^2}{2k^3}(1 + k^2\tau^2).$$

The *power spectrum* $P_{\delta\phi}$ is defined by:

$$P_{\delta\phi}(k) \equiv \frac{k^3}{2\pi^2}\Delta_{\delta\phi}(k).$$

Well outside the horizon, $|k\tau| \ll 1$ and we obtain a scale invariant power spectrum:

$$P_{\delta\phi}(k) \approx \left(\frac{H}{2\pi}\right)^2.$$

In the flat gauge, as we here neglected the metric perturbation, ($\psi = 0$ slicing in (1.19)) and to a linear order, the curvature perturbation is related to the inflaton perturbation by [14]:

$$\zeta = H\frac{\delta\phi}{\dot{\phi}}$$

which gives:

$$P_{\zeta} = \left(\frac{H}{\dot{\phi}}\right)^2 P_{\delta\phi} \approx \frac{1}{2\epsilon}\left(\frac{H}{2\pi}\right)^2 \tag{1.24}$$

using the slow-roll equations (1.13) and (1.14). Observational constraints on ϵ from the CMB are $\epsilon < 0.0097$ at the 95% confidence limit [6]. Therefore, ζ is largely amplified over the fluctuations of ϕ.

These fluctuations are (nearly) Gaussian, by the virtue of the Central Limit theorem. In fact, in this generic single-field slow-roll inflation, the perturbation is constructed from a superposition of Fourier modes with independent random phases. This Gaussianity is well verified with multiple sky surveys. In this case, the power spectrum contains all the information about the primordial perturbation.

1.1.3 Multi-field inflation

The simple inflationary action (1.6) can be extended in many ways. One may consider non-minimal coupling to gravity [15], i.e. direct coupling between the inflaton and the metric, modified gravity [16], non-canonical kinetic term [17], or allowing more than one field. When multiple scalar fields are relevant during inflation, the number of possibilities becomes considerably larger.

If we consider n scalar fields ϕ_i, the Klein-Gordon equation (1.9) becomes:

$$\ddot{\phi}_i - \frac{1}{a^2}\Delta\phi_i + 3H\dot{\phi}_i + \frac{\partial V}{\partial \phi_i}(\phi_1, ..., \phi_n) = 0. \tag{1.25}$$

The pressure and the density write as:

$$\rho = \sum_i \left(\frac{1}{2}\dot{\phi}_i^{\,2} + \frac{1}{2}\frac{(\nabla\phi_i)^2}{a^2} \right) + V(\phi_1, ..., \phi_n), \tag{1.26}$$

$$p = \sum_i \left(\frac{1}{2}\dot{\phi}_i^{\,2} - \frac{1}{6}\frac{(\nabla\phi_i)^2}{a^2} \right) - V(\phi_1, ..., \phi_n). \tag{1.27}$$

Using (1.25) and the previous expressions, (1.4) becomes:

$$\dot{\rho} + 3H(\rho + p) = \sum_i \frac{1}{a^2}\nabla \cdot \left(\dot{\phi}_i \nabla\phi_i \right). \tag{1.28}$$

The continuity equation can be derived from (1.5):

$$\dot{\rho} + 3\tilde{H}(\rho + p) = 0$$

where $\tilde{H} \equiv \dot{\tilde{a}}/\tilde{a} = H - \dot{\zeta}$. Therefore, the primordial curvature perturbation and the scalar fields are linked via:

$$\dot{\zeta} = \frac{\dot{\rho} + 3H(\rho + p)}{3H(\rho + p)} = \frac{1}{a^2}\sum_i \frac{\nabla \cdot \left(\dot{\phi}_i \nabla\phi_i \right)}{3(\rho + p)}. \tag{1.29}$$

The importance of the quantity ζ relies in the fact that it is conserved on super-horizon scales to full non-linear order, provided that the pressure is only a function of the density $p = p(\rho)$ [12].

8

1.1.4 Stochastic inflation

The standard description of inflation, as in (1.20), separates between the homogeneous part that behaves classically, and the perturbations that are small quantum deviations from homogeneity. Stochastic inflation, introduced in [18], takes into account quantum corrections to the background classical trajectory. The basic idea is to split the field into two contributions: short-wavelength (fine-grained) and long-wavelength (coarse-grained), and view the coarse-grained contribution as a nearly classical entity evolving in a "bath" provided by the short-wavelength modes quantum fluctuation. Short and long wavelengths are defined with respect to the Hubble horizon. The result of this theory is that the coarse-grained contribution is modified by the presence of a stochastic term.

The inflaton field is thus written:

$$\phi = \phi_{cg} + \phi_{fg} \tag{1.30}$$

where :

$$\phi_{fg} \equiv \int \frac{d^3\mathbf{k}}{(2\pi)^3} W\left(\frac{k}{\sigma aH}\right) [\phi_\mathbf{k} \hat{a}_\mathbf{k} e^{-i\mathbf{k}\cdot\mathbf{x}} + \text{h.c.}],$$

$$\phi_{cg} \equiv \int \frac{d^3\mathbf{k}}{(2\pi)^3} \left(1 - W\left(\frac{k}{\sigma aH}\right)\right) [\phi_\mathbf{k} \hat{a}_\mathbf{k} e^{-i\mathbf{k}\cdot\mathbf{x}} + \text{h.c.}].$$

W is a window function that allows to select the high modes $k \gg \sigma aH$ for the fine-grained component. It is the component that varies on scales much shorter than the Hubble radius.

We are then interested in the evolution of ϕ_{cg}. In the stochastic picture sub-Hubble modes, which are the quantum-fluctuating modes, are constantly escaping the horizon and source the coarse-grained component. They act as a "noise" for the classical evolution of ϕ_{cg}. Standardly for the coarse-grained piece one can neglect the spatial dependence as it concerns averages over scales larger than the comoving horizon, and in the slow-roll approximation, the time second-derivative is also neglected. By replacing in the Klein-Gordon equation (1.9), the evolution is given by:

$$\ddot{\phi}_{cg} + 3H\dot{\phi}_{cg} - \frac{1}{a^2}\nabla^2\phi_{cg} + V'(\phi_{cg}) = 3Hf(x,t)$$

where:

$$\hat{f}(x,t) \equiv -\frac{1}{3H}\left[\ddot{\phi}_{fg} + 3H\dot{\phi}_{fg} - \frac{1}{a^2}\nabla^2\phi_{fg}\right].$$

When approximating the fine-grained component as a free field, since its dynamics are dominated by the spatial derivatives and the potential effects are negligible, we have in Fourier space:

$$\ddot{\phi}_{fg}(\mathbf{k}, t) + 3H\dot{\phi}_{fg}(\mathbf{k}, t) + \frac{k^2}{a^2}\phi_{fg}(\mathbf{k}, t) = 0.$$

Consequently, as in (1.21), we obtain:

$$\phi_{fg}(\mathbf{k}, \eta) = \frac{H}{\sqrt{2k}}\left(\eta - \frac{i}{k}\right)e^{-ik\eta}$$

which yields:

$$\hat{f}(x, t) = -\frac{1}{3H}\left[\partial_t^2 + 3H\partial_t - \frac{1}{a^2}\nabla^2\right]\int \frac{d^3\mathbf{k}}{(2\pi)^3}W\left(\frac{k}{\sigma aH}\right)[\phi_{\mathbf{k}}\hat{a}_{\mathbf{k}}e^{-i\mathbf{k.k}} + \text{h.c.}]$$

and we obtain considering a Heaviside window function $W\left(\frac{k}{\sigma aH}\right) = \theta(k - \sigma a(t)H)$:

$$\hat{f}(x, t) = \frac{i\sigma aH^2}{\sqrt{2}k^{3/2}}\int \frac{d^3\mathbf{k}}{(2\pi)^3}\delta^D(k - \sigma aH)\left[\hat{a}_{\mathbf{k}}e^{-ik\cdot x} - \text{h.c.}\right].$$

The expectation value and the two-point function of $\hat{f}$ are:

$$\langle\hat{f}(t)\rangle = 0,$$
$$\langle\hat{f}(t)\hat{f}(t')\rangle = \frac{H^3}{4\pi^2}\delta^D(t - t').$$

A critical assumption is to replace the quantum operator $\hat{f}$ by a stochastic variable f. We furthermore assume it has a Gaussian distribution and define the normalized Gaussian noise ξ as:

$$\xi(t) \equiv \frac{2\pi}{H^{3/2}}f.$$

Finally, the evolution of the coarse-grained field is determined by the following Langevin equation:

$$\dot{\phi}_{cg} = -\frac{1}{3H(\phi_{cg})}V'(\phi_{cg}) + \frac{H^{3/2}(\phi_{cg})}{2\pi}\xi(t). \tag{1.31}$$

It is the standard slow-roll equation with an additional stochastic term that represents the quantum fluctuations and their effects on the dynamics. From the Langevin equation we can obtain the Fokker-Planck equation which is related to the probability density function $\mathbb{P}(\phi_{cg}, t)$. It is particularly valuable for non-Gaussianity studies compared to correlation functions as it gives the full statistics of the random field:

$$\partial_t\mathbb{P}(\phi_{cg}, t) = \frac{1}{3}\partial_{\phi_{cg}}\left[\frac{V'}{3H}\mathbb{P}(\phi_{cg}, t)\right] + \frac{1}{8\pi^2}\partial_{\phi_{cg}}\left[H^{3/2}\partial_{\phi_{cg}}\left(H^{3/2}\mathbb{P}(\phi_{cg}, t)\right)\right]. \tag{1.32}$$

1.2 Preheating

A simple variant of chaotic inflation is massless preheating [1], where the inflaton ϕ is coupled to a massless field χ in the potential

$$V(\phi, \chi) = \frac{1}{4}\lambda\phi^4 + \frac{1}{2}g^2\phi^2\chi^2. \tag{1.33}$$

Their dynamics are described by:

$$\ddot{\phi} - \frac{1}{a^2}\Delta\phi + 3H\dot{\phi} + g^2\phi\chi^2 + \lambda\phi^3 = 0,$$

$$\ddot{\chi} - \frac{1}{a^2}\Delta\chi + 3H\dot{\chi} + g^2\phi^2\chi = 0.$$

During inflation, χ is very small and the inflaton evolves as in the standard single-field inflation in a ϕ^4 potential. At the end of inflation, the inflaton reaches the bottom of the potential and starts to oscillate with a decreasing amplitude. The behaviour of this parametric resonance can be classified in terms of the ratio g^2/λ. In terms of the rescaled quantities $\tilde{\phi} \equiv a\phi, \tilde{\chi} \equiv a\chi, d\tilde{\tau} = a^{-1}\lambda^{1/2}A_\phi dt$, the oscillations are approximately described by:

$$\tilde{\phi} = A_\phi \operatorname{cn}(\tilde{\tau}, \frac{1}{2}), \tag{1.34}$$

where A_ϕ is the amplitude of ϕ when the slow-roll is violated and inflation ends. As a consequence of these oscillations, the mass of the χ field $m_\chi \equiv g\phi$ is oscillatory, and in Fourier space at linear level, we have the following Lamé equation:

$$\tilde{\chi}_k'' + \left[\kappa^2 + \frac{g^2}{\lambda}\operatorname{cn}^2(\tilde{\tau}, 1/\sqrt{2})\right]\tilde{\chi}_k = 0, \quad \kappa^2 = \frac{k^2}{\lambda A_\phi^2}. \tag{1.35}$$

where $\prime$ denotes the derivative with respect to the rescaled time $\tilde{\tau}$. Its solutions χ_k may be stable or unstable depending on the values of g^2/λ, which characterizes the strength of the coupling, and κ, which features the vacuum fluctuation momentum. The stability of χ_k can be described by the Floquet index μ such that

$$\tilde{\chi}_k(\tilde{\tau}) = e^{\mu(\kappa, g^2/\lambda)\tilde{\tau}} f(\tilde{\tau}) \tag{1.36}$$

where f is a periodic function. A stability chart can be constructed by numerically solving (1.35) over one $\tilde{\tau}$ unit and determining the corresponding Floquet index. Fig. 1.1 shows that for each value of g^2/λ, there are resonant modes. These are weak when $g^2/\lambda \ll 1$, which means that $g^2/\lambda \gtrsim 1$ is required for preheating to effectively occur. This resonance, where the inflaton transfers its energy to the χ field, results also in rapid particle production and large occupation numbers [1]. Also, the perturbations affect the duration of the resonance and consequently the amount of expansion during this period of preheating. The χ field has therefore an imprint on the primordial curvature perturbations ζ.
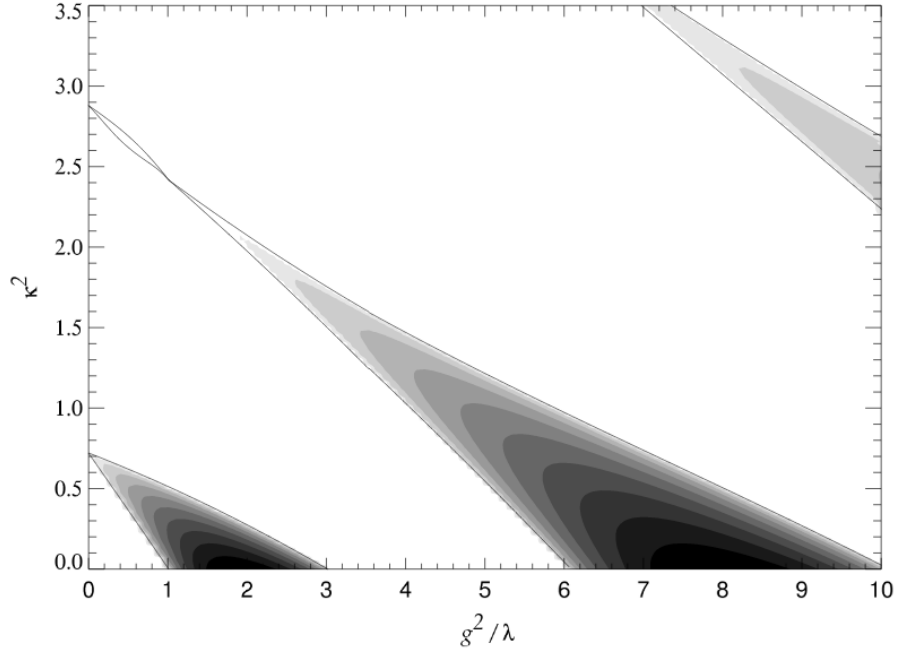
Figure 1.1: Instability chart: the Floquet index as a function of κ^2 and g^2/λ obtained. Darker shades correspond to a higher Floquet index and consequently more instablity [1].

1.3   Contact with observations

The imprint of the inflationary phase during the early universe is observed in the CMB and the LSS. The primordial perturbations can be linked to late-time observables, such as the temperature for the CMB and the matter density for the LSS.

As previously mentioned, the curvature perturbation ζ_k freezes once the corresponding mode k exits the comoving horizon when $k = aH$. In particular, its amplitude is not affected by the (not well-known) physical processes shortly after inflation. To link the primordial perturbations to the a cosmological observable, one needs to take into account the evolution after the horizon re-entry. The relation can be expressed in terms of a transfer function.

As of the fluctuations in the matter distribution of the LSS, the density contrast $\delta(\mathbf{x}, t) \equiv (\rho(\mathbf{x}, t) - \rho(t))/\rho(t)$ can be obtained using a transfer function T that reflects the relative growth of fluctuations during the radiation-dominated era, where the important radiation pressure prevents the rapid growth of fluctuations and $\delta \propto \ln a$, and the matter-dominated era, where the pressure is negligible and the gravitational collapse is more effective as $\delta \propto a$. The calculation of T needs to take into account the

matter, both collisionless dark matter and baryonic plasma, and relativistic particles, i.e. collisionless neutrinos and collisional photons, which makes a complicated mixture that does not behave as a simple fluid. Codes such as `CLASS` [19] and `CAMB` [20] numerically integrate the Boltzmann equations and can provide accurate result of this transfer function that can be related to ζ linearly evolved to a redshift z via:
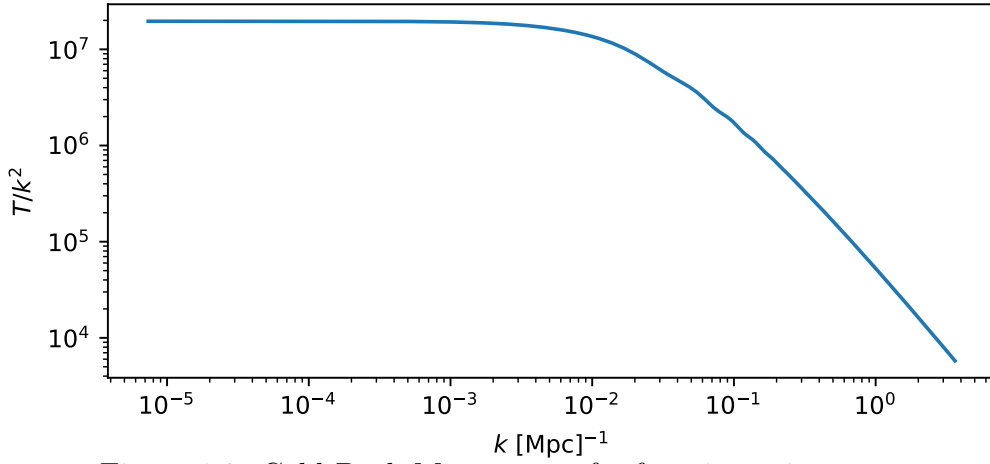
$$\delta(k, z) = T(k, z)\zeta(k). \tag{1.37}$$

Figure 1.2: Cold Dark Matter transfer function using `CAMB` at $z = 0$.

On large scales, as it is shown in Fig. 1.2, the fluctuations are conserved while small-scale perturbations are washed out by the free-streaming damping (fast random particle velocities disperse the fluctuations).

Chapter 2

Generating non-Gaussianity

In the inflationary and post-inflationary scenarios that we explored in the previous chapter, significant non-Gaussianity may arise as a consequence of the fields interaction. Non-Gaussian features in ζ are particularly interesting as their imprints could in principal be directly seen in cosmological observables in the CMB and LSS, though the lower bound on non-Gaussianity still lies a few order of magnitude below the current constraints. As mentioned previously, when the perturbations are drawn from a Gaussian distribution, the power spectrum encodes all the information. This is not the case once the distribution is non-Gaussian. A simple way to obtain additional information on the statistics in this case is to compute higher-order correlation functions such as the bispectrum and the trispectrum. However, these correlation functions by no mean characterize the distribution of the non-Gaussian random field.

The commonly-used local ansatz to parameterize the non-Gaussianity of the primordial curvature perturbation ζ, originally defined in [21], is by a second-order Taylor expansion in the Gaussian component ζ_G:

$$\zeta = \zeta_G + f_{NL}(\zeta_G^2 - \langle \zeta_G^2 \rangle). \tag{2.1}$$

This form of non-Gaussianity is tightly constrained by the recent Planck experiment. This expansion is well justified in the single-field slow-roll inflation model as the non-Gaussian contribution is very small. But in other models, this expansion is not adequate, and a general form of local non-Gaussianity should be considered:

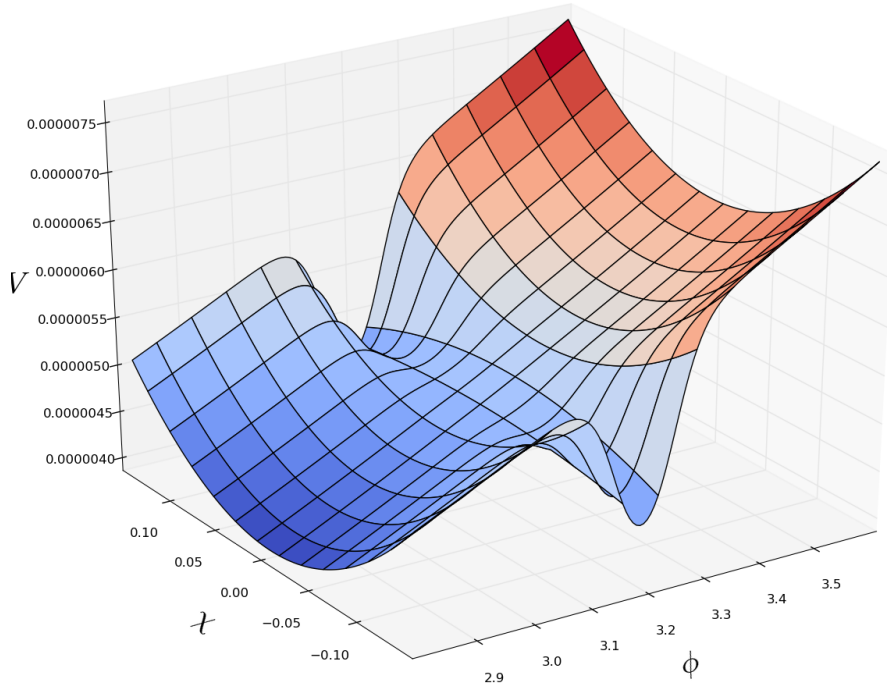$$\zeta = F_{NL}(\zeta_G). \tag{2.2}$$

Figure 2.1: Example of potential instability, by T. Morrison.

We identify mechanisms in models of the previous chapter that generate non-Gaussianity during inflation, when the potential has an instability region (Sec. 2.1.1) and when the stochastic back-reaction is significant (Sec. 2.1.2), and after inflation in the preheating picture (Sec. 2.2).

2.1 During inflation

2.1.1 Potential instability

In a similar picture to the preheating we explored in 1.2, we could consider an instability in the inflaton trajectory by introducing a second field. A particle generation around the instability occurs, and the inflaton resumes its trajectory to end inflation. Unlike some hybrid inflation models [22] where this particle generation ends inflation, here it only occurs in a localized region of the inflaton trajectory. This is expressed by the presence of an additional light field χ during inflation, and the potential writes:

$$V(\phi, \chi) = \frac{1}{2}m_\phi\phi^2 + \Delta V(\phi, \chi) \tag{2.3}$$

and 2.1 shows such a scenario. This instability is accompanied by particle creation

and consequently entropy generation. The correlation between the modes induces a necessarily non-Gaussian contribution to the curvature perturbation.

2.1.2 Stochastic inflation

The background trajectory of the inflaton in the stochastic formalism is corrected by quantum fluctuations of the short-wavelength component of the scalar field. In particular, these corrections are important where the potential is flat, as can be seen in the Langevin equation (1.31). The solutions of the corresponding Focker-Planck equation (1.32) give in general non-Gaussian probability distribution functions of ϕ. For instance, when considering a ϕ^4 inflationary potential, this probability distribution function writes [23]:

$$\mathbb{P}(\phi, t) \propto \frac{1}{\phi^3} \exp\left(-\frac{\phi^{-2} - \phi_{cl}(t)^{-2}}{4\sqrt{2}\lambda((\phi_0/\phi_{cl}(t))^4 - 1)}\right) \tag{2.4}$$

where $\phi_{cl}(t) = \phi_0 \exp\left(-\sqrt{\frac{\lambda}{6\pi}}t\right)$ describes the evolution in the absence of the noise term.

2.2 After inflation

Preheating, as seen in Sec. 1.2, is a mechanism at the end of inflation by which the inflaton quickly transfers its energy to an other field via parametric resonance. As studied in [2], it may leave some imprint on the LSS and could explain the "cold spot" in the CMB radiation [24, 25]. This non-linear resonant preheating induces inhomogeneous variations in the expansion factor, leading to curvature perturbations. At the end of inflation, the light field χ have accumulated quantum fluctuations varying on scales larger than the Hubble radius. On scales shorter than the Hubble scale, χ is homogeneous and isotropic, defining separate universes, each with specific values (spatial averages over the Hubble patch) ϕ_i and χ_i at the end of inflation. The evolution during preheating depending only on these initial conditions, the resulting curvature perturbation[1] on constant energy density hypersurfaces (or constant H by (1.2)) is $\zeta_\chi = \delta \ln a|_H = \delta N(\chi_i)$ where $N \equiv \ln a$ is the number of e-foldings [26]. This is added to the conventional inflation-induced curvature perturbation ζ_ϕ so that $\zeta = \zeta_\phi + \zeta_\chi(\chi_i)$. Using high-accuracy lattice simulations from the end of inflation to the end of preheating by varying the initial condition χ_i for g^2/λ, a non-trivial $\delta N(\chi_i)$ structure is found with a regular pattern of spikes of values of the order of 10^{-5} (Fig.

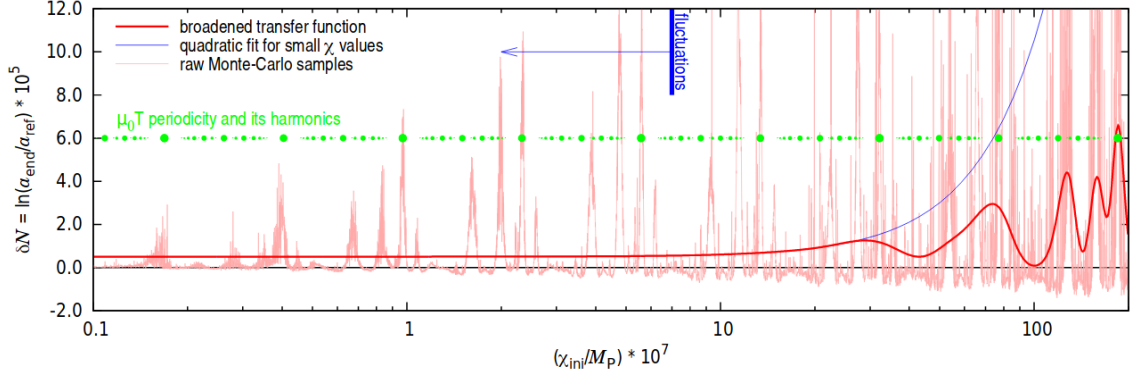[1]ζ as defined in 1.1.2 and [12] corresponds to $-\zeta$ in [26].

Figure 2.2: Value of δN for $g^2/\lambda = 2$ as a function of χ_i [2].

2.2), which corresponds to the order of magnitude of the observed fluctuations in the CMB temperature. It is clear from the blue curve in Fig. 2.2, which is a quadratic fit, how the quadratic expansion (2.1) would not represent such intermittent non-Gaussianity. In [27], the spikes that appear in ζ_χ are simply modeled by spikes generated by a series of log-uniform $\chi_i = \chi_0 e^{nW}$ where n is an integer and W is the Floquet index in units of the inflaton period of oscillation:

$$\zeta_\chi = \sum_n A_n \delta^D \left(\ln \frac{\chi_i}{\chi_0} - nW \right). \tag{2.5}$$

Such non-Gaussianity can produce overabundance in high-redshift $\sim 10^8 M_\odot$ mini-halos and may significantly impact the formation of high-redshift super-massive black holes [27].

Chapter 3

Numerical Simulations

Non-Gaussianity is generated with various inflationary models in different amounts. The curvature perturbation, being conserved and unaffected by immediately-after-inflation physics, is the key quantity that can be related to cosmological observables. Numerical simulations allow to test models and compare them with the observational data. In particular, we are interested here in exploring the effects of different inflationary models on the LSS. For instance, it has been shown that non-Gaussianity in the form of (2.1) produces large correction to galaxy bias in numerical simulations [28]. Here we will present lattice simulations for inflationary models (Sec. 3.1) the mass-Peak Patch algorithm for fast generation of halo catalogues (Sec. 3.2), and different types of the non-linear function F_{NL} (Sec. 3.3).

3.1   Lattice simulations

The evolution of interacting scalar fields in an expanding universe can be simulated using multiple publicly-available codes, each applying a different method to solve the dynamics of the system such as `LATTICEEASY` [29] and `DEFROST` [30] for FLRW universe and `HLattice` [31] for a perturbed FLRW universe. Graduate student T. Morrison currently develops an other high-accuracy lattice simulation for multi-field inflation. In a FLRW metric, the goal is to solve the full equations (1.25):

$$\ddot{\phi}_i - \frac{1}{a^2}\Delta\phi_i + 3H\dot{\phi}_i + \frac{\partial V}{\partial \phi_i}(\phi_1, ..., \phi_n) = 0$$

while enforcing energy conservation using Yoshida symplectic integrator method [32]. The initial conditions are of Bunch-Davies vacuum, i.e. $\phi_i(\mathbf{x}, t = 0) = \bar{\phi}_i(t = 0) + \widehat{\delta\phi}(\mathbf{x}, t = 0)$ and $\dot{\phi}_i(t = 0) = \dot{\bar{\phi}}_i(t = 0) + \widehat{\delta\dot{\phi}}(\mathbf{x}, t = 0)$, where $\widehat{\delta\phi}, \widehat{\delta\dot{\phi}}$ are Gaussian random perturbations. The pressure and energy density have the expressions as seen

in (1.26) and (1.27), and the evolution of the primordial curvature perturbation ζ is computed from the fields using (1.29).

3.2 The mass-Peak Patch algorithm

Traditional N-body simulations are computationally very expensive. And because of the increasing amount of observational data, high-resolution simulations are needed. That is why accelerated methods for LSS simulations are very interesting. The mass-Peak Patch algorithm was first proposed in [33] and had a recent massively-parallel update in [34]. It finds dark matter halos by operating on the the initial density field. It uses Lagrangian perturbation theory to evolve them into their final positions. This gravitational collapse is determined by solving the differential equations of a homogeneous spherical collapse. And this can be summarized in four steps:

- The initial conditions consist of an initial over-density field at redshift $z = 0$. The conventional way to generate them are by convolving a 3D cubic lattice, where each point has a value drawn from a normal distribution, with the linear matter power spectrum for the given cosmological parameters. For this project, this initial over-density will be obtained from non-Gaussian primordial curvature perturbations, as shown in 1.3.

- The density field is smoothed on a number of filter scales to find regions with significant over-density. These regions would be the dark matter halo candidates.

- When a certain region belongs to multiple halo candidates, it can be dealt with by different exclusion methods.

- The halos are finally displaced to their final positions at redshift z.

The mass-Peak Patch software also includes map-making capabilities, including pasted profiles such as thermal and kinetic Sunyaev-Zel'dovich effects, and line profiles of CO and HI.

To relate the output of the lattice simulation (3.1) with the input of the mass-Peak Patch software, the obtained curvature perturbation ζ needs to be converted into an initial density field, and this using the expression (1.37). For this project, the transfer function for the Cold Dark Matter T was computed using `CAMB`, and its shape is shown in Fig. 1.2.

3.3 Primordial curvature perturbation models

The first few runs of 64^3 lattice simulations suggest a negative skewness in the probability distribution function of the primordial curvature perturbation ζ. Larger box size is required to apply mass-Peak Patch and get enough dynamics. We generate a Gaussian random field (App. A) which we transform with a non-linear function F_{NL} as in (2.2) into a non-Gaussian field. The following parameters are considered for all the simulations:

- A lattice size of 256^3 corresponding to a comoving box of 512 Mpc per side, which means that a lattice unit corresponds to 2 Mpc.

- The primordial power spectrum: $P_{\zeta_G} = A_s(k/k_0)^{n_s} k^{-3}$ where $n_s = 0.96$, $A_s = 7.96 \times 10^{-10}$ and $k_0 = 0.02$ Mpc^{-1};

- The reduced Hubble constant: $h = 0.69$.

We distinguish between two kinds of non-Gaussianity: uncorrelated non-Gaussianity that would be generated during preheating for example, and correlated non-Gaussianity as in stochastic inflation.

3.3.1 Uncorrelated non-Gaussianity

If $\zeta_\phi(\mathbf{x})$ designates the Gaussian inflationary, the total non-Gaussian field is

$$\zeta(\mathbf{x}) = \zeta_\phi(\mathbf{x}) + F_{NL}(\zeta_\chi(\mathbf{x}))$$

Unlike [27] where prominence is in the field space (cf. (2.5)), we consider the non-Gaussian contributions as real-space prominence modeled by N_p peaks of Gaussian profile, located at the randomly-drawn prominence positions $\mathbf{x}_p$ and localized over the scale R_p with amplitudes Z_p:

$$F_{NL} = \sum_{p=1}^{N_p} P_p(\mathbf{x} - \mathbf{x_p}) \tag{3.1}$$

where $P_p(\mathbf{x}) = Z_p e^{-\frac{\|\mathbf{x}\|^2}{2R_p^2}}$. Fig. 3.1 shows the real-space realization of such prominence. The power spectrum of ζ is also computed (Fig. 3.2). Depending on the characteristics of the peaks, the power spectrum has a "blob" and the scale around which it is centered depends on the scale of the peaks width. As one would expect, changes on the large scales of the power spectrum corresponds to wider peaks. The effect of these
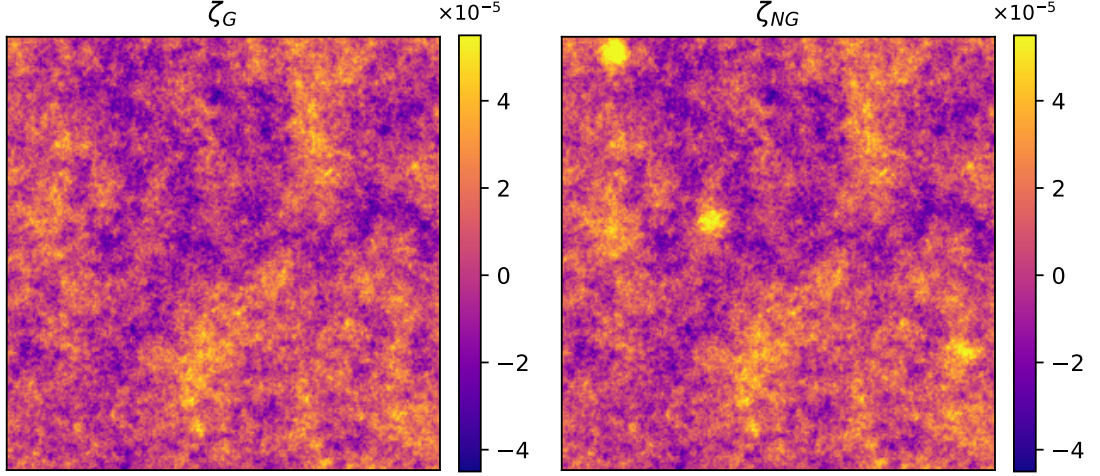
Figure 3.1: A slice of a ζ_G realization on a 256^3 size lattice (left) to which peaks were added (right) such that $N_p = 30$, $Z_p = 8 \times 10^{-5}$ and $R_p = 6$ in lattice units.
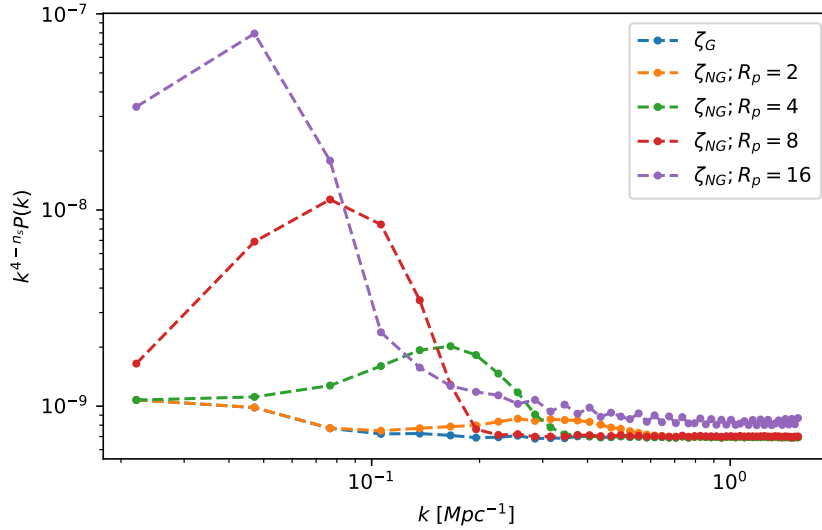

Figure 3.2: Effect of varying the width of the peaks (in lattice unit) on the power spectrum of non-Gaussian ζ with fixed $N_p = 5$, $Z_p = 8 \times 10^{-5}$.
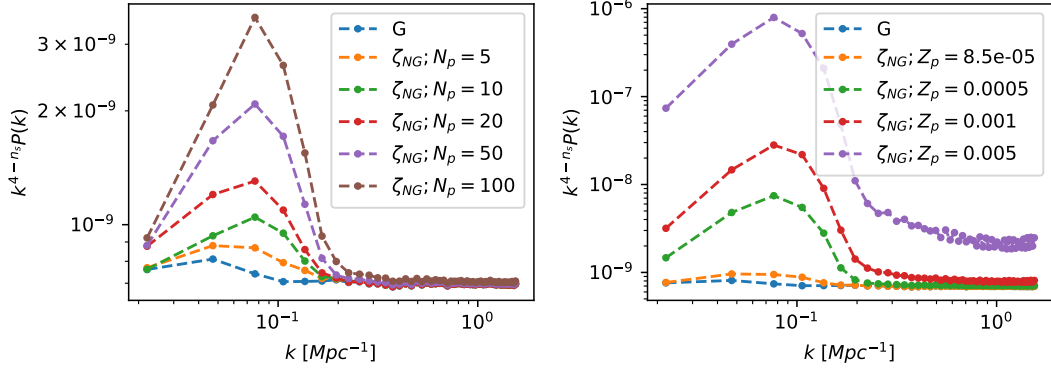
Figure 3.3: Non-Gaussian power spectra by varying the number of peaks N_p (left) and the amplitude Z_p (right).

peaks is localized. The amplitude of the blob also increases with the width, even if Z_p is fixed, because the overall contribution of each Gaussian peak would be given by $Z_p(2\pi R_p^2)^{3/2}$. Modifying the number or the amplitude of the peaks (Fig. 3.3) does not change significantly this characteristic scale. The bispectrum can also be measured (App. A) as it is defined by:

$$\langle \zeta(\mathbf{k_1})\zeta(\mathbf{k_2})\zeta(\mathbf{k_3})\rangle = B(\mathbf{k_1}, \mathbf{k_2}, \mathbf{k_3})\delta^D(\mathbf{k_1} + \mathbf{k_2} + \mathbf{k_3}).$$

Because of the homogeneity and isotropy, it is defined when the three vectors $\mathbf{k_1}, \mathbf{k_2}, \mathbf{k_3}$ form a closed triangle, meaning that it can be parameterized by either the three wavenumbers k_1, k_2, k_3 or k_1, k_2 and θ the angle formed between the two corresponding vectors.
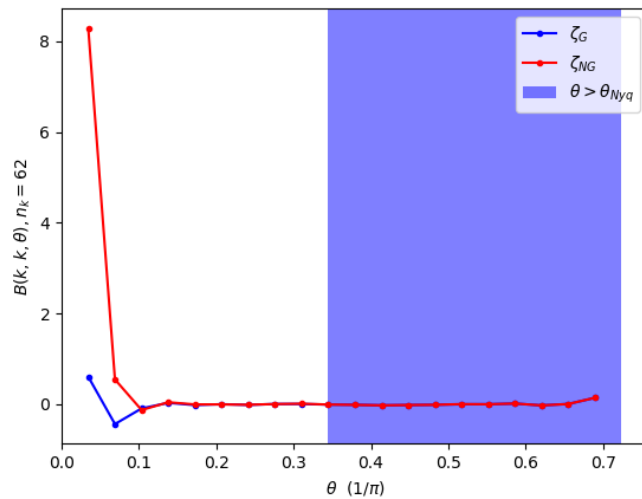

Figure 3.4: Bispectrum as a function of the angle θ, where $k_1 = k_2$. The blue area designate the angles where the third mode is beyond the Nyquist frequency (cf. App. A).
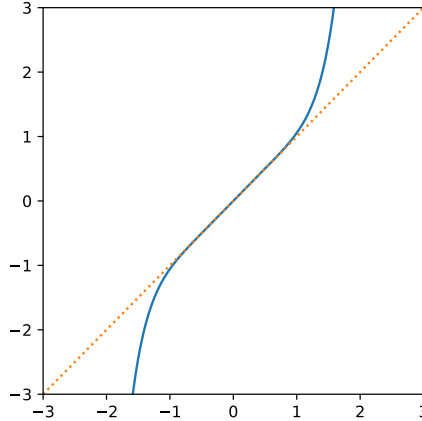
22

Figure 3.5: Symmetric F_{NL} in units of σ.

Fig. 3.4 shows that adding localized peaks gives rise to the local shape of non-Gaussianity [11], which can be seen in the bispectrum when $k_1 \simeq k_2 \gg k_3$, corresponding to $\theta \ll 1$ in Fig. 3.4.

3.3.2 Correlated non-Gaussianity

In the absence of a theoretical expression of F_{NL}, we explore different models and classify them by their effect on the power spectrum and the probability distribution function.

To start with, as non-Gaussianity would appear in regions with uncommonly low or high matter density or temperature (e.g. CMB cold spot, LSS supervoids), one could expect that it comes, due to gravitational collapse, from an unusually high-amplitude peak in the primordial curvature perturbation. We consider F_{NL} of the symmetric shape shown in Fig. 3.5. Values $\lesssim 1$ are not changed when applying this non-linear function, while values > 1 are exponentially boosted. This allows to set a threshold for this amplification, e.g. $\alpha\sigma$, with σ the standard deviation of the field. Note that this function, being symmetric, does not bias the mean of field and keeps it centered. We are mostly interested in peaks that are "compactly " formed, meaning that one isolated pixel with an excessively high value for instance is not relevant as it will most probably be washed out in the dynamics of later evolution. To avoid the influence of these outliers, the field can be smoothed over a scale R_f by convolving it with a window function as follows:

$$\zeta_{R_f}(\mathbf{k}) = W_f(\mathbf{k}; R_f)\zeta(\mathbf{k}).$$

We here use a Gaussian filter which is given by $W_G(\mathbf{k}; R_f) = e^{-(R_f k)^2/2}$. Smoothing
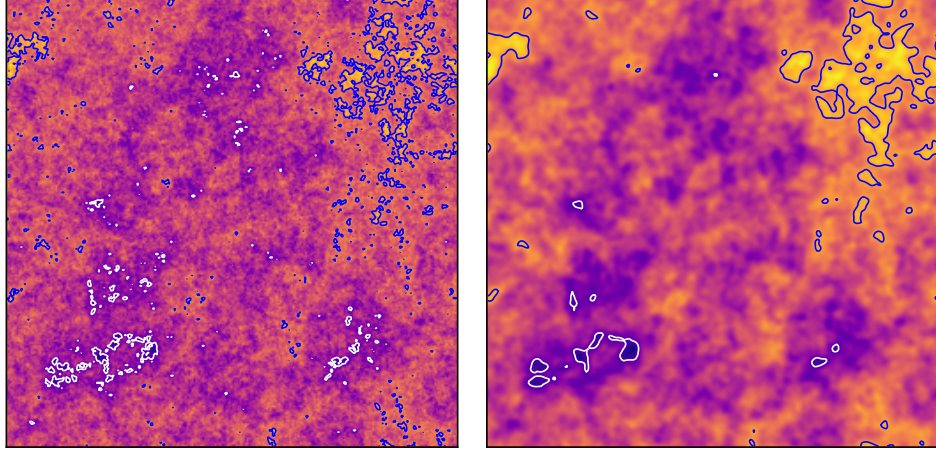
Figure 3.6: Slice of a Gaussian realization with contours at $\pm 2\sigma_G$ (left) and its smoothed version over $R_f = 16$ Mpc with contours at $\pm 2\sigma_{G,f}$ (right).
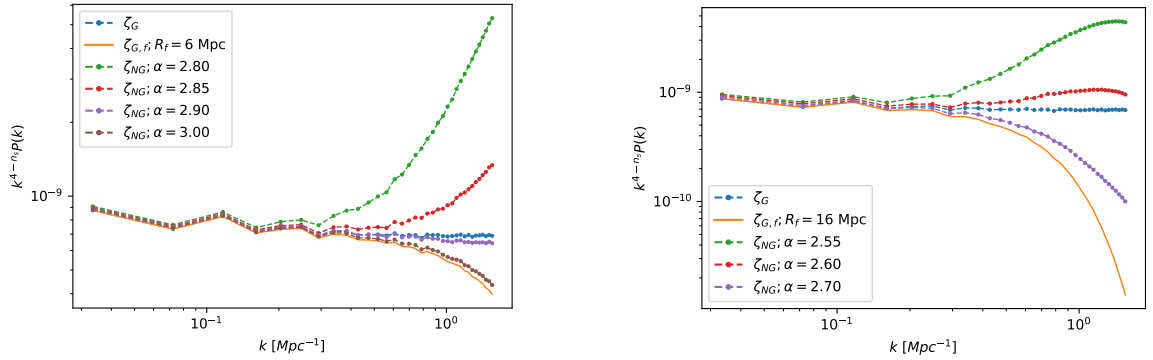

Figure 3.7: Power spectrum of non-Gaussian field using F_{NL} of Fig. 3.5 applied on smoothed Gaussian field over $R_f = 6$ Mpc (left) and $R_f = 16$ (right).
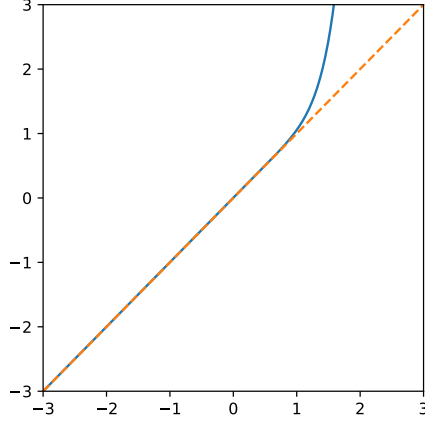
Figure 3.8: Asymmetric F_{NL} in units of σ.

the field damps the high-frequency modes of the power spectrum as seen in Fig. 3.7. It also gives a more compact structure of the peaks, as seen in Fig. 3.6, and applying our F_{NL} would very much less boost the outliers. Fig. 3.7 shows that the statistics of the field are not significantly changed on large scales. The peaks above $\alpha\sigma_f$ for the considered α are rare and the influence increases with lower α.

If we consider an asymmetric F_{NL} that corresponds to a peak boosting for positive values only (Fig. 3.8). Unlike the previous case, we here need to subtract the mean of the obtained field to maintain a zero-mean ζ. Its effect on the power spectrum is very similar to the symmetric F_{NL}, although less powerful as it requires lower threshold $\alpha\sigma$ to get the same order of magnitude of the modification.
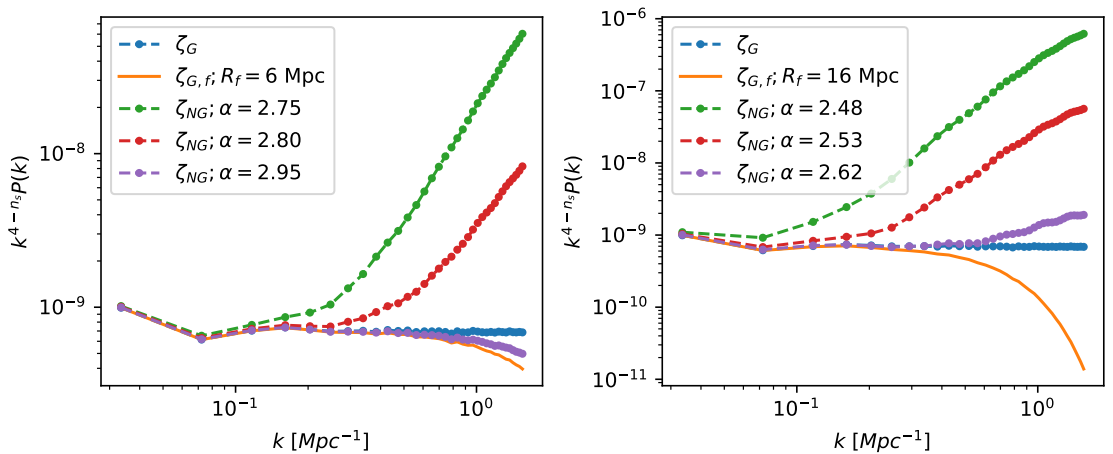

Figure 3.9: Power spectrum of non-Gaussian field using F_{NL} of Fig. 3.8 applied on smoothed Gaussian field over $R_f = 6$ Mpc (left) and $R_f = 16$ (right).
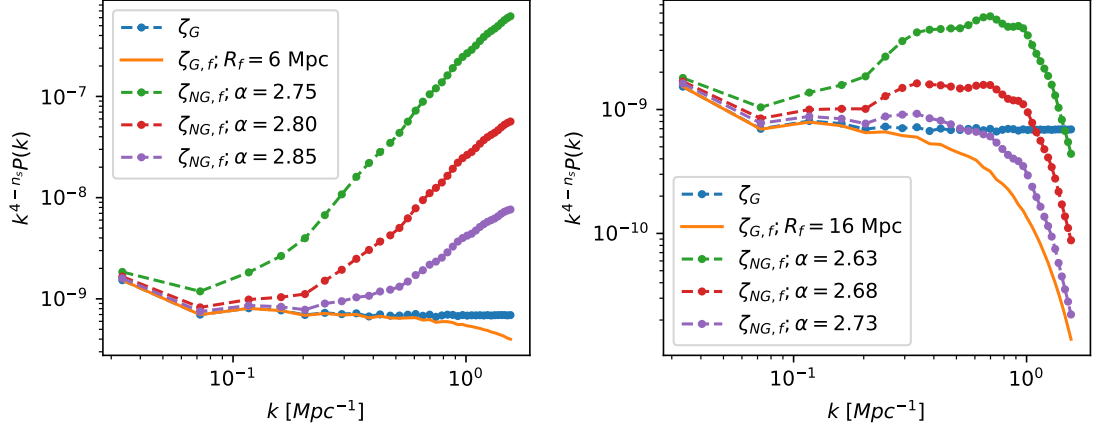
25

Figure 3.10: Power spectra of smoothed non-Gaussian fields over the same initial smoothing scales $R_f = 6 Mpc$ (left) and $R_f = 16 Mpc$ (right).

Examining real-space slices of the non-Gaussian ζ shows that the effect of outliers could still be significant, even with the preliminary smoothing. Filtering the obtained field on the same initial filtering scale should give us an idea of the effect these outliers have on the power spectrum. A comparison between Fig. 3.10 and Fig. 3.9 shows that when the larger post-smoothing scale is used, high-frequency modes for do have an important influence on the power spectrum. Smoothing the field afterwards damps these modes and the resulting non-Gaussianity produces a feature similar to a blob around $k \approx 0.4$ Mpc^{-1}. This corresponds to the scale of the filtering and it can be deduced that the prominent peaks that appear with this type of F_{NL} are of that scale.
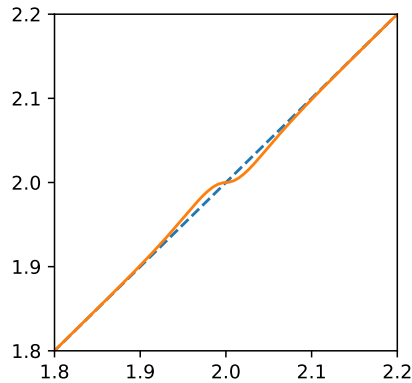

Figure 3.11: F_{NL} with a slow-variation on a given range, and approximately matches the first bisector everywhere else.

Let us now consider the effect of some F_{NL} functions on the probability distribu-

tion function. From the real-space realization of the symmetric F_{NL}, we can expect thicker tails as more high values are taken by the field. As for the asymmetric F_{NL} it negatively skews it because of the amount of the positively high values. These changes affect the whole shape of the distribution. We now consider a non-linear function with a localized effect on the probability distribution, for example a localized bump, as such feature could easily be spotted on the data. A bump would mean higher realization probability for a certain range of values $[\zeta_1, \zeta_2]$. To achieve this, an F_{NL} varying very slowly on $[\zeta_1, \zeta_2]$ compared to the first bisector $(y = x)$ would transfer that range into a narrower range $[F_{NL}(\zeta_1), F_{NL}(\zeta_2)]$ such that $|F_{NL}(\zeta_2) - F_{NL}(\zeta_1)| \ll |\zeta_2 - \zeta_1|$, meaning that values the narrow range have a higher probability of realization. Outside this region, so as the rest of the distribution remains unchanged, the variation of F_{NL} needs to be as close as possible of that of the first bisector as in Fig. 3.11.
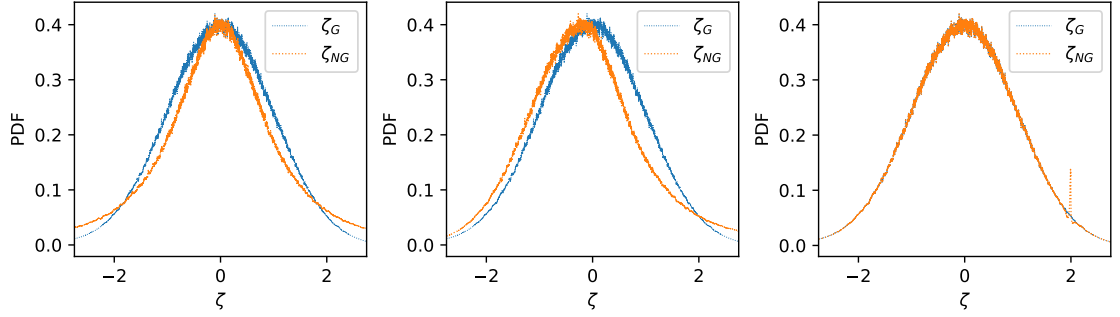

Figure 3.12: Probability distribution functions of symmetric F_{NL} (left), asymmetric F_{NL} (center) and F_{NL} of Fig. 3.11 (right).

Chapter 4

Independent Component Analysis

As mentioned before, the bispectrum is a simple measure of non-Gaussianity. But it cannot decisively assess that a signal is non-Gaussian, as the construction of a non-Gaussian variable with a vanishing bispectrum is not impossible. Here we explore a potential alternative to characterize non-Gaussianity in a signal by applying ICA as one if its features is to separate non-Gaussian components. The difficulty with applying ICA is that it requires as many signal measurements as the components we want to extract. The common example of ICA application is speech separation: if three people are speaking at the same time and we want to separate their speeches, we would need three microphones at different locations. The measurements would be a linear combination of the to-be-separated components. In cosmological applications, for instance, extracting non-Gaussian components from the CMB with ICA would in principle require an other source of information. This underdetermined problem of ICA is a very difficult one and different approaches are possible. In this chapter, as a preliminary work, we assume that we have enough measurements to separate the components, and we only treat the case of one-dimensional signals, which could be applied for example for $\zeta = \zeta_\phi + \zeta_\chi$ in the preheating scenario. The algorithm of ICA separation is introduced (Sec. 4.1), applied in some situations of interest (Sec. 4.2) and results are summarized (Sec. 4.3).

4.1   ICA and measures of non-Gaussianity

This section is based on [35]. ICA considers the problem of recovering a signal $\mathbf{s}$ provided a measurement $\mathbf{x}$ which is a linear transformation of $\mathbf{s}$ as follows :

$$\mathbf{x} = \mathbf{A}\mathbf{s}. \tag{4.1}$$

In the following, we suppose that the signal $\mathbf{s}$ consists of n_c components: a Gaussian noise and $n_c - 1$ non-Gaussian signals, so that its dimension is $n_s \times n_c$, where n_s is the number of samples. ICA estimates, by maximizing the non-Gaussianity of each component, a matrix $\mathbf{W}$ such that it recovers $\mathbf{s}$ from $\mathbf{x}$:

$$\mathbf{s} \approx \mathbf{W}\mathbf{x}.$$

4.1.1 Degeneracies

From (4.1) we see that there are ambiguities that will hold, since only $\mathbf{x}$ is known:

- The variances of the source signals cannot be recovered. The signals are estimated up to a multiplicative factor.

- The order of the components cannot be recovered, as $\mathbf{s}$ and $\mathbf{A}$ are both unknown and the order can be permuted without changing $\mathbf{x}$.

4.1.2 Measures of non-Gaussianity

Kurtosis: Kurtosis is a simple measure of non-Gaussianity as it can be directly estimated from a measured sample. However, it can be very sensitive to outliers and may depend only on a few observations in the tail of the distribution.

Negentropy: The differential entropy H of a random variable $\mathbf{y}$ with a distribution function f is defined by:

$$H(\mathbf{y}) = - \int f(\mathbf{y}') \ln f(\mathbf{y}') d\mathbf{y}'.$$

One can show that a Gaussian variable has the largest differential entropy H among all random variables of equal variance. We can define negentropy J as:

$$J(\mathbf{y}) = H(\mathbf{y_G}) - H(\mathbf{y}) \tag{4.2}$$

where $\mathbf{y_G}$ is a Gaussian variable with the same covariance matrix as $\mathbf{y}$. Negentropy is then a measure of non-Gaussianity as it is positive and equals zero when $\mathbf{y}$ is Gaussian, but it is difficult to compute in practice as it requires the specific probability distribution function of $\mathbf{y}$.

Approximations of negentropy: In practice the negentropy is estimated using the following formula [35]:

$$J(\mathbf{y}) \propto (E[G(\mathbf{y})] - E[G(\mathbf{y_G})])^2 \qquad (4.3)$$

where G is a non-quadratic function. In general, one of these three functions is used:

- $G(y) = \frac{1}{\alpha} \ln \cosh(\alpha y)$ where $1 \leq \alpha \leq 2$ is the commonly-used function in ICA algorithms. We call this method 'logcosh'.

- $G(y) = -e^{-y^2/2}$ is good when the components are highly super-Gaussian or when robustness is very important.

- $G(y) = y^4$ recovers the case where the non-Gaussianity measure is kurtosis. Its usage is only well justified when the components are sub-Gaussian and there are no outliers.

4.1.3 How does ICA work?

To estimate one component, `FastICA` finds a direction $\mathbf{w}$ that maximizes the considered non-Gaussianity measure $J(\mathbf{w^\mathsf{T}x})$. This maximization is based on a fixed-point iteration scheme, and the steps of the algorithm are:

1. Choose an initial (random) unit vector $\mathbf{w}$.

2. Compute: $\mathbf{w_{New}} = E[\mathbf{x}G'(\mathbf{w^\mathsf{T}x})] - E[G''(\mathbf{w^\mathsf{T}x})]\mathbf{w}$.

3. Update: $\mathbf{w} \leftarrow \mathbf{w_{New}} / \|\mathbf{w_{New}}\|$.

4. Go back to 2 until convergence.

To estimate multiple component, an orthogonalization is needed to avoid the convergence to the same solution. It can be achieved by either a *Gram-Schmidt orthogonalization* (deflationary `FastICA`) or a *symmetric orthogonalization* (symmetric/parallel `FastICA`).

In [36], an experimental comparison shows that symmetric `FastICA` using the 'logcosh' approximation of negentropy is close to the best algorithms.

4.2 Tests

Tests are carried to examine the signal recovery in some cases of interest by `FastICA`. Unless mentioned otherwise, the deflationary version of `FastICA` is used for the following tests.

For each test a plot of the original sources, which are then randomly mixed and put through `FastICA`, and plots of the recovered signals are presented. As mentioned previously, `FastICA` relies on the maximization of a non-Gaussianity measure to estimate the components. I focus particularly on comparing the results when kurtosis measure and 'logcosh' negentropy measure are used. For these tests, the following values are used:

- Number of components: $n_c = 3$

- Number of samples: $n_s = 1000$

- Tolerance threshold: $\epsilon = 10^{-4}$

- Maximum number of iterations: $n_{max} = 100$

Test 1:

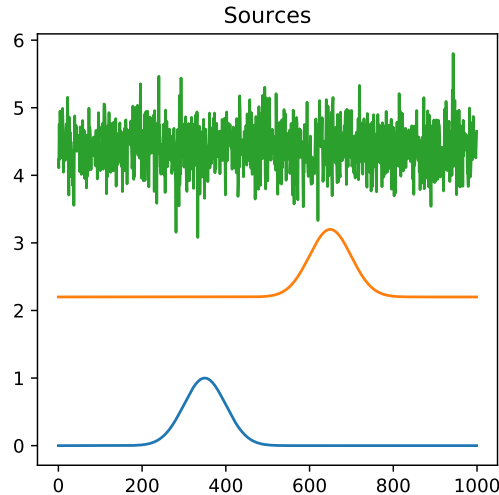We start by applying ICA on a mixture of the following three signals.
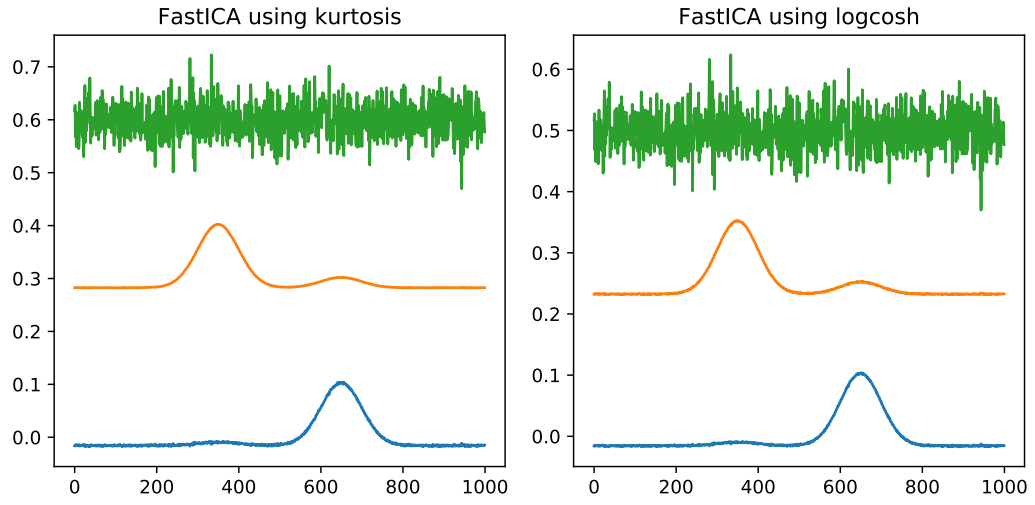

Figure 4.1: Two peaks with the same width

31

Figure 4.2: Recovered signals

For two Gaussian peaks with the same characteristics and distant from each other, `FastICA` recovers well the signals with small residuals.

Test 2:

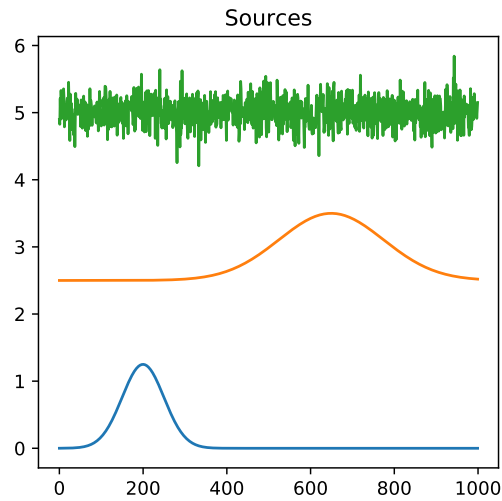Here we consider two separated peaks with different widths.

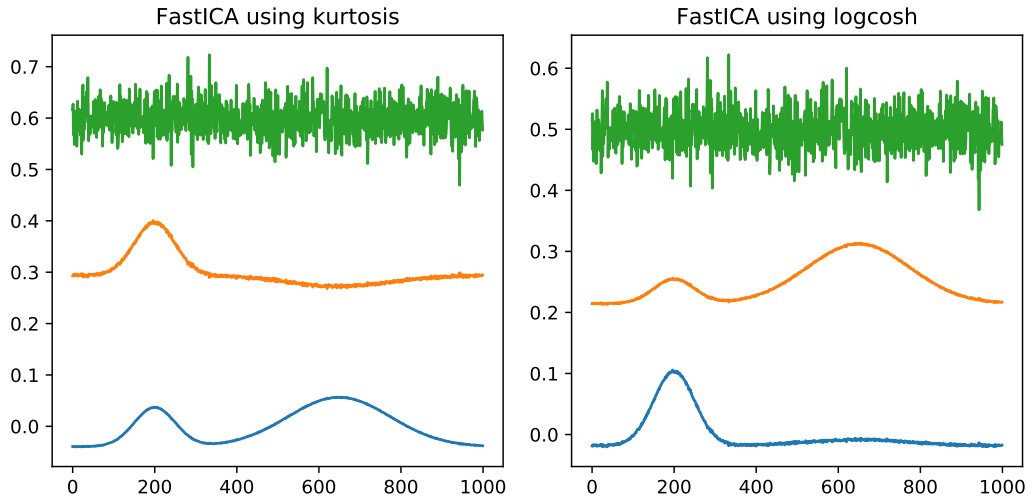Figure 4.3: Two peaks with different widths

Figure 4.4: Recovered signals

FastICA is unable to recover the exact original signals. Instead it extracts the narrow peak and a linear combination of the two peaked signals. As for the Gaussian noise, it is well recovered.

Test 3:

We consider now two interfering peaks, a wide one and a narrow one, where the latter is located at the tail of the wider peak.
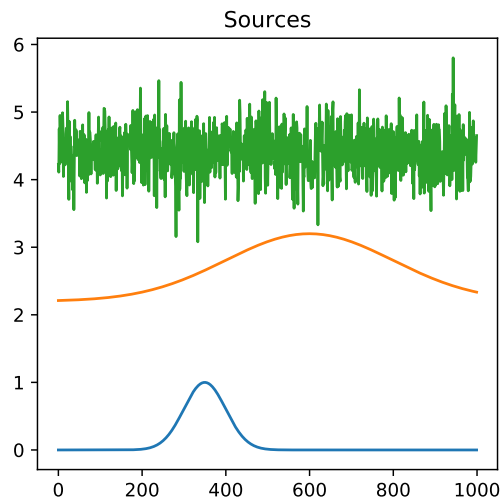

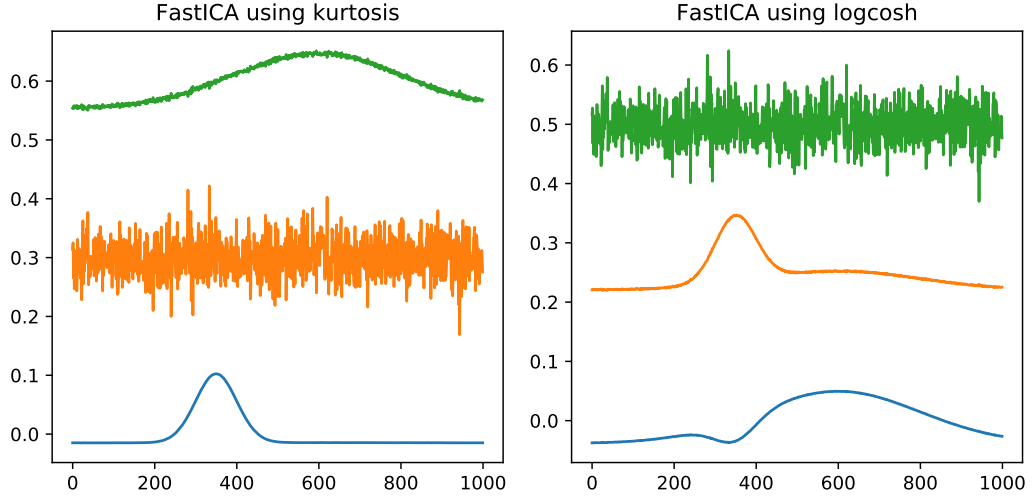Figure 4.5: Two peaks with different width

Figure 4.6: Recovered signals

While the 'logcosh' method converges to a linear combination of the original sources, using the kurtosis here gives better results, although with some convergence difficulties. The Gaussian noise is, here again, well estimated. On the other hand, the symmetric `FastICA` actually separates well the components for both considered non-Gaussianity measures in this case as shows the plot bellow.
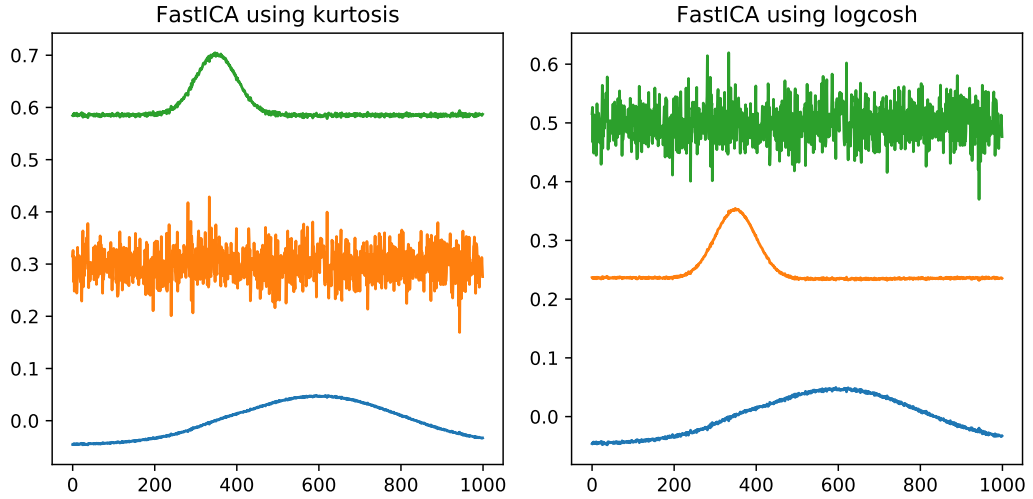

Figure 4.7: Recovered signals by the symmetric `FastICA`

Test 4:

We consider two nested peak, i.e., a narrow peak positioned near the center of the wide peak, and see how `FastICA` estimates these signals.
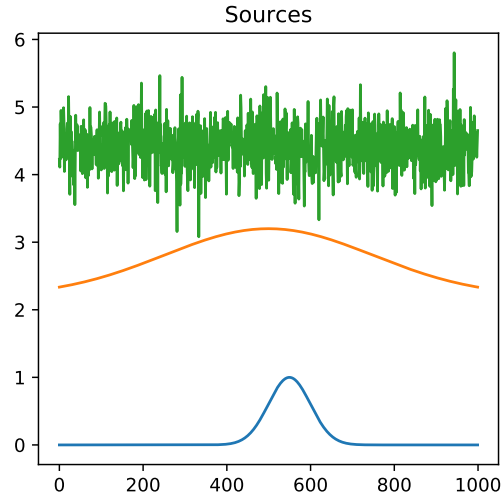
Figure 4.8: Two nested peaks
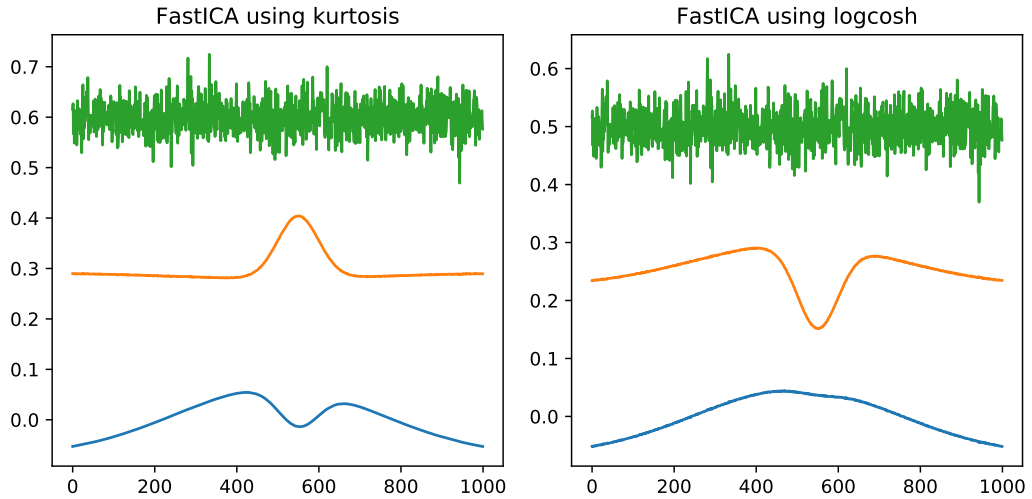
Figure 4.9: Recovered signals

Using kurtosis, `FastICA` separates quite well the narrow peak while the 'logcosh' negentropy allows a good estimation of the wider peak. In both cases, the other signals are linear combinations of the narrow peak and wide peak signals.

Test 5:

An extreme case is considered to test the robustness of kurtosis and 'logcosh' to outliers: very narrow peaks are added with high amplitudes compared to the rest of the signal.
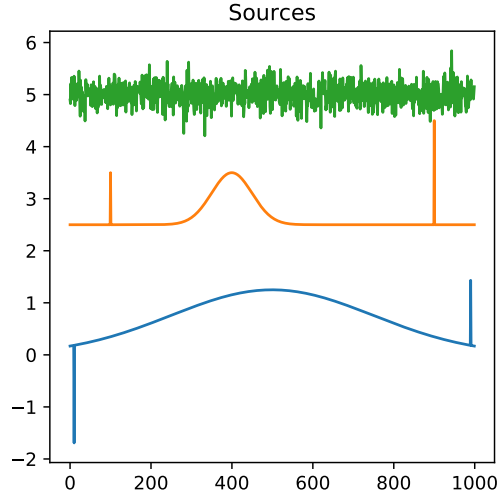
Figure 4.10: Source signals
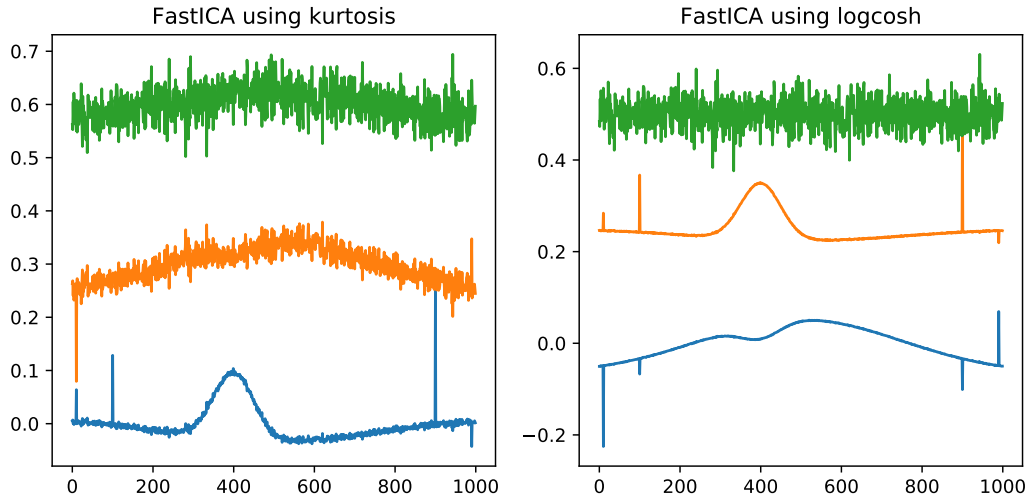
Figure 4.11: Recovered signals

With the presence of extreme values in the input signals, the kurtosis method fails to separate the signals from the Gaussian noise. As mentioned before, the kurtosis may depend only on few values that are in the tail of the distribution. We see here that the 'logcosh' measure of non-Gaussianity is indeed robust to these outliers and still estimates well the Gaussian component and separates the very narrow peaks from the Gaussian signal.

4.3 Summary of results

In almost all the cases, `FastICA` estimates well the Gaussian signal. The non-Gaussian component estimation depends on the non-Gaussianity measure and on the characteristics of the peaks. Here we considered kurtosis and an approximation of negentropy to separate the components. With both measures, we do not always recover the original shape of the non-Gaussian signals, but rather some linear combinations. As we might expect, the sensitivity of the kurtosis to the outliers can lead to a failure to separate the Gaussian signal from the non-Gaussian one as seen in test 5, which is avoided when using the 'logcosh' approximation of negentropy.

Conclusion

In this report we reviewed inflation and the generation of primordial curvature perturbations. The simplest model of inflation predicts a Gaussian distribution of the curvature perturbation to a high level. Current observational bounds allow significant deviations from this Gaussianity. The common way to describe non-Gaussianity in the literature is the quadratic expression with the parameter f_{NL}. Such parameterization does not match the non-Gaussianity that emerges from many inflationary models.

Stochastic inflation is a framework where the quantum fluctuations during inflation modify the inflaton background trajectory contributing to non-Gaussian ζ. In the preheating picture the light non-inflaton field is the source of non-Gaussianity and that gives an uncorrelated contribution to the curvature perturbation that emerged during inflation. Part of the project was to relate the primordial curvature perturbation issued from lattice simulations to the mass-Peak Patch software using `CAMB` to obtain catalogue halos and sky maps for each considered inflationary scenario.

In addition, non-quadratic local non-Gaussianity models were discussed as well as their induced statistical effects in terms of the real-space realizations, power spectra, bispectra and probability distribution functions. The local property of non-Gaussianity (e.g. peaks appearing in bounded regions of space) can appear in real-space, in in Fourier space or even field-space. We treated the real-space prominence in two cases: first the randomly-generated peaks on the lattice are uncorrelated with the underlying Gaussian field ζ_G, and second the ζ_G peaks over a certain threshold are boosted, producing therefore peaks fully correlated with ζ.

We also explored Independent Component Analysis as a potential way to extract non-Gaussian components of a signal and tested it under some strong assumptions, and obtained interesting results. Next will be to adapt this algorithm for cosmological applications, which correspond to underdetermined ICA. Also, with the full pipeline from the inflationary model to the cosmological observables, generating full-sky mocks are of great interest to study the imprints of these various models.

Appendix A

Statistical tools

On a regular discrete cubic lattice with N^3 pixels per side and a volume L^3, the Fourier transform of a real-space quantity $Q(\mathbf{x})$ is:

$$Q(\mathbf{k}) = \frac{1}{L^3} \sum_{\mathbf{x}} Q(\mathbf{x}) e^{i\mathbf{k} \cdot \mathbf{x}}$$

and the inverse Fourier transform:

$$Q(\mathbf{x}) = \frac{L}{N^3} \sum_{\mathbf{k}} Q(\mathbf{k}) e^{-i\mathbf{k} \cdot \mathbf{x}}. \tag{A.1}$$

To generate a Gaussian random field with a given power spectrum $P(k)$, we can just compute

$$f_{\mathbf{k}} = \sum \hat{a}_{\mathbf{k}} \sqrt{P(k)} e^{-i\mathbf{k} \cdot \mathbf{x}}$$

where $\hat{a}_{\mathbf{k}}$ is a zero-mean standard normal deviate, and inverse-Fourier transform it using (A.1).

The power spectrum of $Q(\mathbf{x})$, defined in (1.23), can be directly measured from the lattice. It is the angular average of the square modulus of the Fourier transform of Q. In fact, if $|Q(\mathbf{k})|^2 = f(k, \theta, \phi)$, the measured power spectrum is:

$$P(k) \approx \frac{1}{4\pi} \int f(k, \theta, \phi) \sin \theta d\theta d\phi. \tag{A.2}$$

This is achieved in practice by considering k bins of a width Δk, e.g. $\text{Bin}(k) \equiv \left\{ \mathbf{k}', k - \frac{\pi}{L} \le |\mathbf{k}'| < k + \frac{\pi}{L} \right\}$, and average $|Q(\mathbf{k})|^2$ over each as

$$\langle |Q(\mathbf{k})|^2 \rangle = \frac{1}{|\text{Bin}(k)|} \sum_{\mathbf{k}' \in \text{Bin}(k)} |Q(\mathbf{k}')|^2. \tag{A.3}$$

A second method, which was used in this project, to compute the bispectrum relies on, instead of averaging over bins which is increasingly complicated and computationally expensive beyond the power spectrum (e.g. triangular bins for the bispectrum, quandrilateral bins for the trispectrum...), approximating these bin averages by using Fourier transforms [37]. In particular, for the bispectrum:

$$B(k_1, k_2, k_3) \approx \frac{L^3}{N^6} \frac{\sum_{\mathbf{x}} Z(\mathbf{x}, k_1) Z(\mathbf{x}, k_2) Z(\mathbf{x}, k_3)}{\sum_{\mathbf{x}} I(\mathbf{x}, k_1) I(\mathbf{x}, k_2) I(\mathbf{x}, k_3)} \tag{A.4}$$

where:

$$Z(\mathbf{x}, k) = \sum_{\mathbf{k}' \in \text{Bin}(k)} \zeta(\mathbf{k}') e^{i\mathbf{k}'\mathbf{x}},$$

$$I(\mathbf{x}, k) = \sum_{\mathbf{k}' \in \text{Bin}(k)} e^{i\mathbf{k}'\mathbf{x}}.$$

Note that $\frac{1}{N^3} \sum_{\mathbf{x}} I(\mathbf{x}, k_1) I(\mathbf{x}, k_2) I(\mathbf{x}, k_3)$ corresponds to the number of triangles with sides in the bin $\text{Bin}(k)$. This method can be used a fast estimator of the power spectrum and even higher-order polyspectra.

As the *Nyquist theorem* states, the smallest wavelength that can be resolved on two pixels on the lattice is $2L/N$. This corresponds to an upper limit on the modes, called the Nyquist mode:

$$k_{Nyq} \equiv \frac{2\pi}{2L/N} = \frac{N\pi}{L}.$$

The power spectrum calculations used in the report do not include modes $k > k_{Nyq}$.

To compute the probability distribution function of Q, we first increasingly sort its values on the lattice $[Q_0, Q_1, ..., Q_{N^3-1}]$. The cumulative distribution function is obtained for each value Q_n of this array as:

$$\text{CDF}(Q_n) \equiv \mathbb{P}(Q < Q_n) = \frac{n}{N^3 - 1}.$$

Differentiation of the cumulative distribution function gives the probability distribution function, which means:

$$\text{PDF}(Q_n) \equiv \frac{\partial \text{CDF}}{\partial Q}(Q_n) \approx \frac{\text{CDF}(Q_{n+1}) - \text{CDF}(Q_n)}{Q_{n+1} - Q_n} = \frac{1}{(N^3 - 1)(Q_{n+1} - Q_n)}.$$

Bibliography

[1] Patrick B. Greene, Lev Kofman, Andrei D. Linde, and Alexei A. Starobinsky. Structure of resonance in preheating after inflation. *Phys. Rev.*, D56:6175–6192, 1997.

[2] J. Richard Bond, Andrei V. Frolov, Zhiqi Huang, and Lev Kofman. Non-Gaussian Spikes from Chaotic Billiards in Inflation Preheating. *Phys. Rev. Lett.*, 103:071301, 2009.

[3] Alan H. Guth. Inflationary universe: A possible solution to the horizon and flatness problems. *Phys. Rev. D*, 23:347–356, Jan 1981.

[4] Alan H. Guth and So-Young Pi. Fluctuations in the new inflationary universe. *Phys. Rev. Lett.*, 49:1110–1113, Oct 1982.

[5] A.A. Starobinsky. Dynamics of phase transition in the new inflationary universe scenario and generation of perturbations. *Physics Letters B*, 117(3):175 – 178, 1982.

[6] Y. Akrami et al. Planck 2018 results. X. Constraints on inflation. 2018.

[7] Xi Kang, P. Norberg, and J. Silk. Can large-scale structure probe CMB-constrained non-Gaussianity? *Mon. Not. Roy. Astron. Soc.*, 376:343–347, 2007.

[8] E. Sefusatti, M. Crocce, and V. Desjacques. The matter bispectrum in N-body simulations with non-Gaussian initial conditions. *MNRAS*, 406(2):1014–1028, Aug 2010.

[9] Emiliano Sefusatti, Martin Crocce, and Vincent Desjacques. The Halo Bispectrum in N-body Simulations with non-Gaussian Initial Conditions. *Mon. Not. Roy. Astron. Soc.*, 425:2903, 2012.

[10] Christian Wagner, Licia Verde, and Lotfi Boubekeur. N-body simulations with generic non-Gaussian initial conditions I: power spectrum and halo mass function. *JCAP*, 2010(10):022, Oct 2010.

[11] Tomo Takahashi. Primordial non-Gaussianity and the inflationary Universe. *Progress of Theoretical and Experimental Physics*, 2014(6), 06 2014.

[12] David H. Lyth, Karim A. Malik, and Misao Sasaki. A General proof of the conservation of the curvature perturbation. *JCAP*, 0505:004, 2005.

[13] David H. Lyth and Andrew R. Liddle. *The primordial density perturbation: Cosmology, inflation and the origin of structure.* 2009.

[14] Juan Martin Maldacena. Non-Gaussian features of primordial fluctuations in single field inflationary models. *JHEP*, 05:013, 2003.

[15] Mark P. Hertzberg. On Inflation with Non-minimal Coupling. *JHEP*, 11:023, 2010.

[16] S. Nojiri, S. D. Odintsov, and V. K. Oikonomou. Modified Gravity Theories on a Nutshell: Inflation, Bounce and Late-time Evolution. *Phys. Rept.*, 692:1–104, 2017.

[17] C. Armendariz-Picon, T. Damour, and Viatcheslav F. Mukhanov. k - inflation. *Phys. Lett.*, B458:209–218, 1999.

[18] Alexei A. Starobinsky. Stochastic De Sitter (inflationary) stage in the early universe. *Lect. Notes Phys.*, 246:107–126, 1986.

[19] Diego Blas, Julien Lesgourgues, and Thomas Tram. The cosmic linear anisotropy solving system (CLASS). part II: Approximation schemes. *Journal of Cosmology and Astroparticle Physics*, 2011(07):034–034, 07 2011.

[20] Antony Lewis, Anthony Challinor, and Anthony Lasenby. Efficient computation of CMB anisotropies in closed FRW models. *Astrophys. J.*, 538:473–476, 2000.

[21] Eiichiro Komatsu and David N. Spergel. The Cosmic Microwave Background bispectrum as a test of the physics of inflation and probe of the astrophysics of the low-redshift Universe. In *Recent developments in theoretical and experimental general relativity, gravitation and relativistic field theories. Proceedings, 9th Marcel Grossmann Meeting, MG'9, Rome, Italy, July 2-8, 2000. Pts. A-C*, pages 2009–2012, 2000.

[22] Andrei D. Linde. Hybrid inflation. *Phys. Rev.*, D49:748–754, 1994.

[23] James S. Bullock and Joel R. Primack. NonGaussian fluctuations and primordial black holes from inflation. *Phys. Rev.*, D55:7423–7439, 1997.

[24] Marcos Cruz, L. Cayon, E. Martinez-Gonzalez, P. Vielva, and J. Jin. The non-gaussian cold spot in the 3-year wmap data. *Astrophys. J.*, 655:11–20, 2007.

[25] M. Cruz, E. Martinez-Gonzalez, P. Vielva, and L. Cayon. Detection of a non-gaussian spot in wmap. *Mon. Not. Roy. Astron. Soc.*, 356:29–40, 2005.

[26] D. S. Salopek and J. R. Bond. Nonlinear evolution of long-wavelength metric fluctuations in inflationary models. *Phys. Rev. D*, 42:3936–3962, 12 1990.

[27] Zhiqi Huang. High-redshift minihaloes from modulated preheating. *Phys. Rev.*, D99(10):103537, 2019.

[28] Neal Dalal, Olivier Dore, Dragan Huterer, and Alexander Shirokov. The imprints of primordial non-gaussianities on large-scale structure: scale dependent bias and abundance of virialized objects. *Phys. Rev.*, D77:123514, 2008.

[29] Gary N. Felder and Igor Tkachev. LATTICEEASY: A Program for lattice simulations of scalar fields in an expanding universe. *Comput. Phys. Commun.*, 178:929–932, 2008.

[30] Andrei V. Frolov. DEFROST: A New Code for Simulating Preheating after Inflation. *JCAP*, 0811:009, 2008.

[31] Zhiqi Huang. The Art of Lattice and Gravity Waves from Preheating. *Phys. Rev.*, D83:123509, 2011.

[32] Haruo Yoshida. Construction of higher order symplectic integrators. *Physics Letters A*, 150(5):262 – 268, 1990.

[33] John Richard Bond and S T Meyers. The peak-patch picture of cosmic catalogs. i. algorithms. *Astrophysical Journal Supplement*, 103:1, Mar 1996.

[34] George Stein, Marcelo A. Alvarez, and J. Richard Bond. The mass-Peak Patch algorithm for fast generation of deep all-sky dark matter halo catalogues and its N-Body validation. *Mon. Not. Roy. Astron. Soc.*, 483(2):2236–2250, 2019.

[35] Aapo Hyvärinen, Juha Karhunen, and Erkki Oja. *Independent Component Analysis*. Wiley-Interscience, 2001.

[36] Xavier Giannakopoulos, Juha Karhunen, and Erkki Oja. An experimental comparison of neural algorithms for independent component analysis and blind separation. *International Journal of Neural Systems*, 09(02):99–114, 1999.

[37] Catherine A Watkinson, Suman Majumdar, Jonathan R. Pritchard, and Rajesh Mondal. A fast estimator for the bispectrum and beyond – a practical method for measuring non-Gaussianity in 21-cm maps. *Mon. Not. Roy. Astron. Soc.*, 472(2):2436–2446, 2017.